Nanoscale Horizons

Inhomogeneous energy landscape in $LaAlO_3/SrTiO_3$ nanostructures

Journal:	*Nanoscale Horizons*
Manuscript ID	NH-COM-03-2019-000188.R1
Article Type:	Communication
Date Submitted by the Author:	16-May-2019
Complete List of Authors:	Nethwewala, Aditi; University of Pittsburgh, Department of Physics and Astronomy Lee, Hyungwoo; University of Wisconsin-Madison, Materials Science and Engineering Briggeman, Megan; University of Pittsburgh, Department of Physics and Astronomy Tang, Yuhe; University of Pittsburgh, Department of Physics and Astronomy Li, Jianan; University of Pittsburgh, Department of Physics and Astronomy Lee, Jungwoo; University of Wisconsin-Madison, Materials Science and Engineering Eom, Chang-Beom; University of Wisconsin Madison Irvin, Patrick; University of Pittsburgh, Physics and Astronomy Levy, Jeremy; University of Pittsburgh

Conceptual Insights:

In this manuscript we describe a unique conducting AFM lithography technique that we use to define crossed electron waveguides (nanocrosses) at the interface of $LaAlO_3$ (LAO) and $SrTiO_3$ (STO). We use the nanocrosses as probes of the 2D electron system found at the LAO/STO interface. We find that the transport is inhomogeneous but highly reproducible. Previous reports have often attributed anisotropic transport at the LAO/STO interface to multiband nature of the 2D electron system (2DES). However, that theory fails to provide a satisfactory explanation in all regimes, for example at small magnetic fields. We believe the inhomogeneity is related to the ferroelastic domain structure found in STO, which is artificially defined during the nanocross writing procedure. Since the nanocross geometry allows us to artificially define the ferroelastic domain structure in STO, we can correlate the observed inhomogeneities to the domain configuration across the nanocross through a simple domain model, providing insights into potential mechanisms. The inhomogeneities are observed across the nanocross at a given chemical potential and magnetic field, eliminating the role of the multiband nature of 2DES. The nanocross provides new insights into the transport properties of strongly correlated STO-based systems in one-dimension and the influence of ferroelastic domains.

Inhomogeneous energy landscape in $LaAlO_3/SrTiO_3$ nanostructures

Aditi Nethwewala,[ab] Hyungwoo Lee,[c] Megan Briggeman,[ab] Yuhe Tang,[ab] Jianan Li,[ab] Jungwoo Lee,[c] Chang-Beom Eom,[c] Patrick Irvin,[ab] Jeremy Levy*[ab]

[a] *Department of Physics and Astronomy, University of Pittsburgh, Pittsburgh, PA 15260, USA.*
[b] *Pittsburgh Quantum Institute, Pittsburgh, PA, 15260 USA.*
[c] *Department of Materials Science and Engineering, University of Wisconsin-Madison, Madison, WI 53706, USA.*
[*] *To whom correspondence should be addressed. E-mail: jlevy@pitt.edu*

Abstract: $SrTiO_3$-based heterointerfaces exhibit gate-tunable superconductivity, magnetism, and several other properties that can be programmed at nanoscale dimensions using conductive atomic force microscopy (c-AFM). Spatially resolved measurements indicate that intrinsic structural distortions in the $SrTiO_3$ layer can profoundly influence the transport characteristics. Here, we report low temperature transport properties of quasi-1D, cross-shaped electron waveguides, "nanocrosses", created at the $LaAlO_3/SrTiO_3$ interface using c-AFM lithography. Inhomogeneities in the electronic band structure of the four arms are observed that are highly reproducible over several device writing/measurement cycles, provided that the writing is performed at the same location on the sample. A proposed ferroelastic domain configuration near the nanocross can provide a mechanism for the observed inhomogeneities. Our model suggests that the three-dimensional ferroelastic domain structure of $SrTiO_3$ near the $LaAlO_3/SrTiO_3$ interface can significantly and reproducibly affect the transport properties of the interface. The nanocross geometry can also serve as a building block for understanding 1D electron physics of $LaAlO_3/SrTiO_3$ heterostructures.

Introduction

The quasi-two-dimensional electron system (2DES) in $SrTiO_3$ based heterointerfaces combines the abilities of semiconductor systems with rich correlated electron physics.[1, 2] In particular, the 2DES at the $LaAlO_3/SrTiO_3$ (LAO/STO) interface[3] shows a range of gate-tunable correlated electronic phases including superconductivity,[4, 5] magnetism,[6] and electron-electron interactions[7], as well as other important interactions like spin-orbit coupling.[8, 9] The ability to create nanoscale devices at the interface[10] has added a new level of control and richness to the LAO/STO system. Quasi-one-dimensional (1D) nanostructures created at the interface exhibit a variety of intriguing phenomena like ballistic transport[11] and electron pairing without superconductivity.[11, 12] Additionally, many electronic properties of the 2DES are claimed to be 1D in nature.[13-15] However, despite intense recent attention, a detailed understanding of these phenomena remains elusive. A possible key to revealing the hidden physics may be to understand the microscopic nature of transport at the LAO/STO interface, and the factors influencing it.

Many of the interesting electronic properties appear linked to the structural phases of STO. The cubic unit cell of STO undergoes an antiferrodistortive phase transition[16] at 105 K to the tetragonal state, forming ferroelastic domains along the X, Y or Z direction. Recent experimental studies suggest the 2DES interacts with the ferroelastic domains, significantly affecting the transport properties at the LAO/STO interface.[14, 15, 17-20] Scanning single electron transistor[19] (SET) microscopy and superconducting quantum interference device (SQUID) microscopy measurements[18] provide direct evidence of enhanced conductivity along the domain walls. Scanning SET measurements[19] further show that while the X and Y domains share a similar surface potential, the Z domains have a higher surface potential, varying by approximately 1 mV. Thus, the Z domains in STO can be argued to form the conducting regions at the interface whereas the X and Y domains define the insulating states. The influence of ferroelastic domains has been shown to affect various properties of the superconducting state at the LAO/STO interface.[13, 21] In reports by Pai et al,[13] it has been suggested that ferroelastic domain boundaries play an important role behind the pairing mechanism at the interface, leading to the one-dimensional nature of superconductivity[13] and non-superconducting paired states.[11-13]

The coupling between the transport properties and ferroelastic domains can potentially account for a variety of unusual transport signatures such as the existence of gate-tunable and magnetic-field tunable anisotropic magnetoresistance[14, 22-25], and inconsistencies between Shubnikov de-Haas (SdH) and Hall measurements of carrier density in STO-based systems[20]. Cheng et al. have argued[20] that SdH-like oscillations, in STO-based systems arise due to magnetic depopulation of subbands, and are actually manifestations of naturally-formed 1D channels at the ferroelastic domain boundaries.

While the ferroelastic domains are expected to influence the transport properties, they can also be artificially defined in LAO/STO heterostructures using conductive-atomic force microscope (c-AFM) lithography.[10, 26] Piezoelectric force microscopy imaging experiments[27] on conductive LAO/STO nanostructures have shown that conducting paths written by c-AFM lithography are elongated along the Z-axis at room temperature. The pre-seeded domain configurations are expected to be preserved at low temperatures, so that conducting and insulating regions at the interface naturally coincide with the ferroelastic domain boundaries.

Here, we investigate the low-temperature transport properties of quasi-1D, cross-shaped electron waveguides (“nanocrosses”) formed at the LAO/STO interface using c-AFM lithography.[26] The presence of the intersection defines both Z-X and Z-Y domain boundaries in the system, in close proximity. The symmetric and multiterminal nature of the nanocross allows us to measure the four-terminal longitudinal measurements along several directions, providing insight into the nature of electron transport in complex 1D systems and its corresponding relation to the ferroelastic domain configuration. Hence, the nanocross geometry provides a plausible microscopic picture of transport at the interface and the role of ferroelastic domains on it.

Experimental

A thin film of LAO (3.4-unit cell) is grown on STO using pulsed laser deposition using growth conditions described elsewhere.[28] Electrical contact is made to the interface by depositing Ti/Au (4 nm/25 nm) electrodes surrounding a given "canvas". The main device is subsequently written on the canvas using c-AFM lithography.[10, 26] Conducting paths are created by applying a positive bias to the c-AFM tip, locally protonating the LAO surface, thereby attracting conducting electrons to the interface.[29] The insulating state is restored by applying negative voltages to the tip, locally deprotonating the surface. The lithography technique is reversible and does not involve any physical modulation of the interface. Low-temperature transport measurements are conducted by applying an out-of-plane magnetic field $\vec{B} = B\hat{z}$ near the base temperature of the dilution refrigerator, $T = 50$ mK.

The nanocross (depicted schematically in **Fig. 1**) consists of two perpendicular 1 μm-long line segments surrounded by four highly transparent[11] tunnel barriers (width ~ 30 nm). The tunnel barriers decouple the nanocross from the terminal leads, allowing the electron density of the nanocross to be tuned by the proximal sidegate V_{sg}. The position of the side gate does not influence the nature and tuning of the tunnel barriers.[11] The nanocross orientation with respect to the actual crystallographic direction (ϕ) is controlled but not represented in the schematic illustrations. The precise device layout and corresponding sample topography are illustrated in **Fig. S1**.

The six distinct current paths for the nanocross are illustrated in **Fig. 2 (a-f)**. There are two straight paths, namely, the horizontal (H) and vertical (V) configurations, and four "L shaped" paths (L_1, L_2, L_3, L_4). For each of these configurations, current I is sourced between the source (I^+) and drain (I^-) while voltages (V^+/V^-) are measured to produce four-terminal longitudinal conductance measurements as a function of applied gate voltages V_{sg} and external magnetic field B (see **Fig. 2 (a-f)**).

Results and discussion

The conductance of an electron waveguide primarily depends on the chemical potential μ and the applied magnetic field $\vec{B}$. The chemical potential of the device can be tuned with the proximal side gate V_{sg}. For a quasi-1D straight electron waveguide[11] written at the LAO/STO interface, the conductance is quantized near integer values of e^2/h in the presence of an external magnetic field. The transport properties of LAO/STO heterostructures in 1D regime is intrinsically different from semiconductors systems like GaAs/AlGaAs. When patterned into 1D channels, repulsive interactions at semiconductor interfaces generally leads to a significant drop in mobility due to enhanced impurity or interface scattering.[30-32] However, unlike semiconductor systems, attractive electron-electron interactions in LAO/STO heterostructures are believed to strongly suppress the scattering mechanism[11]. The zero bias longitudinal conductance $G = dI/dV$ for the six configurations of the nanocross of Device A is

recorded as a function of the chemical potential μ for a sequence of magnetic fields between $B = 0$ and $B = 8$ T (**Fig. 2 (g-l)**). Quantized conduction steps are observed in each of the six configurations, indicating the existence of ballistic transport. Transport in the nanocross remains ballistic till the lowest magnetic fields. The fractional values of the conductance quantization steps are attributed to weak interference effects due to the multiterminal nature of the device. Conductance quantization steps at values between e^2/h and $2e^2/h$ are associated with a paired electron state.[11, 12] Pairing is generally observed up to a critical "pairing field", B_p which can be anywhere in the range $1 - 10$ T.

To reveal more information about the electronic structure within the nanocross, we calculate the transconductance $dG/d\mu$ and plot it as an intensity map as a function of B and μ. Transconductance spectra of the six configurations for Device A are plotted in **Fig. 2 (m-r)**. A peak in the transconductance marks the chemical potential at which a new subband contributes to transport (the subband bottom). The subbands are further separated by regions where the conductance is quantized ($dG/d\mu \rightarrow 0$). Insight into the nature of electron transport of the nanocross comes from arranging the transconductance spectra for the six configurations in decreasing order of the lowest subband bottom (**Fig. 2 (m-r)**). The following observations can be made:

1. The transconductance spectra can be sorted into three groups based on similarity (see **Fig. 2**) (labeled I, II, III in **Fig. 2**). The group with the highest gate voltage threshold for conduction has the largest number of members (three for group I in the given case) and vice versa.
2. Within each group, the configurations share a common source (I^+) or drain (I^-). For example, group I shares a common arm a_1, group II shares a common arm a_2. The last group III is not distinctly associated with either of the two remaining arms (a_3 , a_4).
3. The pairing field (B_p) differs among the three groups of the nanocross. B_p is lowest for group I ~ 3 T, followed by group II and III (the pairing field exceeds 8 T).
4. The specific pattern of subband minima is highly reproducible from one c-AFM writing to the next, provided the nanocross is written in the same position and orientation on the LAO/STO sample (**Fig. S2**, **Fig. S3**).
5. Changing the orientation of the nanocross otherwise at the same position on the canvas, changes the nature of the transconductance spectra of each group (**Fig. 3**). However, the transconductance spectra of the rotated nanocross can still be identically sorted into groups I, II and III like that of Device A.
6. We also observe some additional features (marked by green arrows) in the transconductance spectra of the six configurations of the nanocross (see **Fig. 2**). These features are not present in the transconductance spectra of most quasi-1D straight electron waveguides and are symmetric as a function of the magnetic field.

To get a finer picture of the transport properties across the nanocross, we plot the conductance of the vertical configuration (G_v) as an intensity map as a function of B and μ (**Fig. 4(a)**). Plots of conductance (G_v) versus magnetic field (B) are shown for selected values of chemical potential μ (**Fig. 4(b)**). Magnetic depopulation signatures are clearly observed, similar to those previously reported in straight electron waveguides.[20] Superimposed on the magnetic depopulation signatures are prominent quasi-oscillatory features (marked by black lines in **Fig. 4(b)**), which are reproducible at a specific chemical potential but vary from one device to the next and change with magnetic field. The quasi-oscillatory features are identified as manifestations of universal conductance fluctuations (UCF).[33-35] UCF also accounts for the additional features (mentioned in the observations above) in the transconductance spectra of the nanocross. Quantum interference effects like UCF have been previously reported in mesoscopic LAO/STO devices created by other techniques.[35]

Notably, the quasi-oscillatory features are particularly magnified for certain values of G_v (denoted by black lines in **Fig. 4(b)**) independent of the value of chemical potential and magnetic field ($B < 4$ T for $\mu = 0.59$ meV and $B > 4$ T for $\mu = 0.67$ meV). In order to understand this relationship, the standard deviation of G_v (σG_v) is plotted versus the mean value of G_v (**Fig. 4(c)).** The procedure for obtaining the standard deviation and mean value of G_v is described in the supplementary section (**Fig. S4**). Dips in the standard deviation (shaded pink) are clearly correlated with stable quantized values in the G_v versus μ plot (shaded pink in **Fig. 4(d)**), especially at low overall conductance values. Similar dips in conductance fluctuation (σG_v) have been previously attributed to saturation of channel transmission in ballistic point contacts.[36, 37] The magnification of quasi-oscillatory features near the subband minima can be understood from a simple picture where the subband bottom of the nanowire acts like a "beam splitter" in the nanocross giving rise to magnified quantum interference effects. Similar phenomena have also been observed in mesoscopic LAO/STO devices.[38]

Magnetotransport measurements across the nanocross shows that there is significant inhomogeneity in the transport properties at the interface. In spite of extending 1 μm along two dimensions, the electronic band structure of the four arms of the nanocross exhibits pronounced inhomogeneity. To understand how inhomogeneities may arise in the nominally symmetric nanocross, we consider a simplified model (**Fig. 5(a)**) of how ferroelastic domains are expected to align with a nanocross device that is oriented along major crystallographic directions. The ferroelastic domains in STO can be oriented along the X (100), Y (010) or Z (001) crystalline direction, separated by nanometer-scale domain walls, with domain boundaries aligned according to the domain tiling rules (**Fig. S5**).[19] Specifically, near the surface of STO, the boundary between Z and X domains should lie at 0°, between Z and Y domains at 90° and between X and Y domains at 45° or 135°. While the lowest energy configuration is expected to have similar domain configuration across the four arms of the nanocross (**Fig. 5(a)**), far off boundary conditions may lead to an expansion or contraction of the X and Y domains, which can be parameterized by the angles $\delta_i, i = 1, \ldots, 4$ (**Fig. 5(b)**). Movement of the X and

Y domains is expected to produce a strain within the conductive nanowires. This in turn will affect the electronic band structure of the nanowire, shifting energy subbands up or down, accordingly. Thus, each arm of the nanocross is expected to have a unique electronic band structure, represented by its corresponding transconductance spectra. The measured conduction band energy difference (~1 meV) between Z domain regions compared with X or Y domains[19] is generally in good agreement with theoretical calculations[39], setting the overall scale of the energetics due to structural distortions of this type. Further, we consider the effect of rotation of the nanocross on the ferroelastic domain configuration across it. **Fig. 5(c)** shows a possible ferroelastic domain configuration for a nanocross rotated by an angle of 65 ° with respect to the (100) crystallographic direction, taking into account known tiling rules. The contiguous size and shape of the X and Y domains is expected to be altered by the rotation of the nanocross, although the domain configuration across each arm should remain identical in the lowest energy configuration. Additionally, as previously mentioned, expansion or contraction of the X and Y domains from the lowest energy configuration (parameterized by the angles $\delta_i', i = 1, \dots, 4$ in **Fig. 5(d)**) can similarly lead to inhomogeneities across the four arms of the rotated nanocross.

We recall that all the configurations within a given group share a common current-carrying lead (I^+ or I^-) (**Fig. 2**). We consider this common arm to be the least conducting lead of the group, namely arm a_1 for group I, arm a_2 for group II and arm a_3 or a_4 for group III (**Fig. 2**). The least conducting lead dominates the conductance of a given configuration. Furthermore, electronic states within the nanocross are extended and delocalized. Together, these two assumptions help to account for observed similarities in transconductance spectra observed among all configurations within a group. Additionally, since the bottom of the first subband is at the highest value of μ for group I, followed by groups II and III respectively, arm a_1 possibly represents the least conducting lead of the nanocross whereas arm a_3 or a_4 represents the most conducting leads.

Finally, we extend the ferroelastic domain model to understand the nature of electron pairing across the nanocross. The pairing field, B_p, is found to vary among the three groups of the transconductance spectra. We have reported similar variations in the value of B_p from one c-AFM writing to next in straight electron waveguides and SETs.[11, 12] However, due to limitations of the device geometry, these variations were not measured across a single device at a given chemical potential and magnetic field till date. In reports by Pai et al,[13] it has been suggested that the pairing mechanism at the LAO/STO interface is mediated by the ferroelastic domain boundaries. As previously mentioned, with c-AFM lithography we define the Z-X and Z-Y domain boundaries along the edges of the nanocross. Further, with the given domain model, we discussed the possibility of the X and Y domains deviating from their lowest energy configuration, producing an unequal strain across the nanocross arms. The resulting strain can shift the energy difference between the Z-X and Z-Y domains, differing along the four arms of the nanocross. Hence, these

inhomogeneities can potentially account for the observed differences in the pairing field, B_p, across the four arms of the nanocross.

The experimental results reported here support the idea that the nanocross geometry, by its two-dimensional nature, constrains ferroelastic domains in the vicinity of the cross, thereby stabilizing the transport properties. Devices created at the same spatial position on the sample (and orientation) are highly reproducible in their magnetotransport properties from one c-AFM writing to the next. When grouped on the basis of decreasing threshold for conductance, the transport characteristics exhibit very similar transconductance spectra for all three devices. It was further shown that rotating the angle of the nanocross ϕ with respect to crystallographic axis (without changing its location) significantly alters the transport properties of the nanocross. Future studies, possibly coupled with theoretical modeling (e.g., phase-field simulations[40, 41]), may help to establish a more microscopic understanding of the interrelationships between electronic band structure, nanostructure geometry, and ferroelastic domain structure for $LaAlO_3/SrTiO_3$ nanostructures created by c-AFM lithography.

Acknowledgements

We acknowledge useful discussions with Yun-Yi Pai. This work is supported by Vannevar Bush Faculty Fellowship ONR grant N00014-15-1-2847 (J.L.). The work at University of Wisconsin-Madison was supported by the National Science Foundation (DMR-1629270) and the Air Force Office of Scientific Research (FA9550-15–1-0334).

Figures

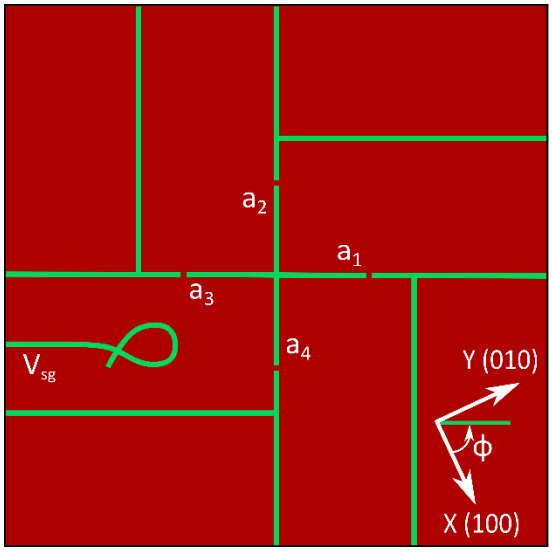

Fig. 1 Schematic of $LaAlO_3/SrTiO_3$ nanocross written using c-AFM lithography. Four barriers of width ~ 30 nm surround the main channels of length ~ 1000 nm forming a nanocross which can be tuned by a proximal sidegate V_{sg}. Angle ϕ denotes the relative position of the nanocross with respect to the crystallographic direction.

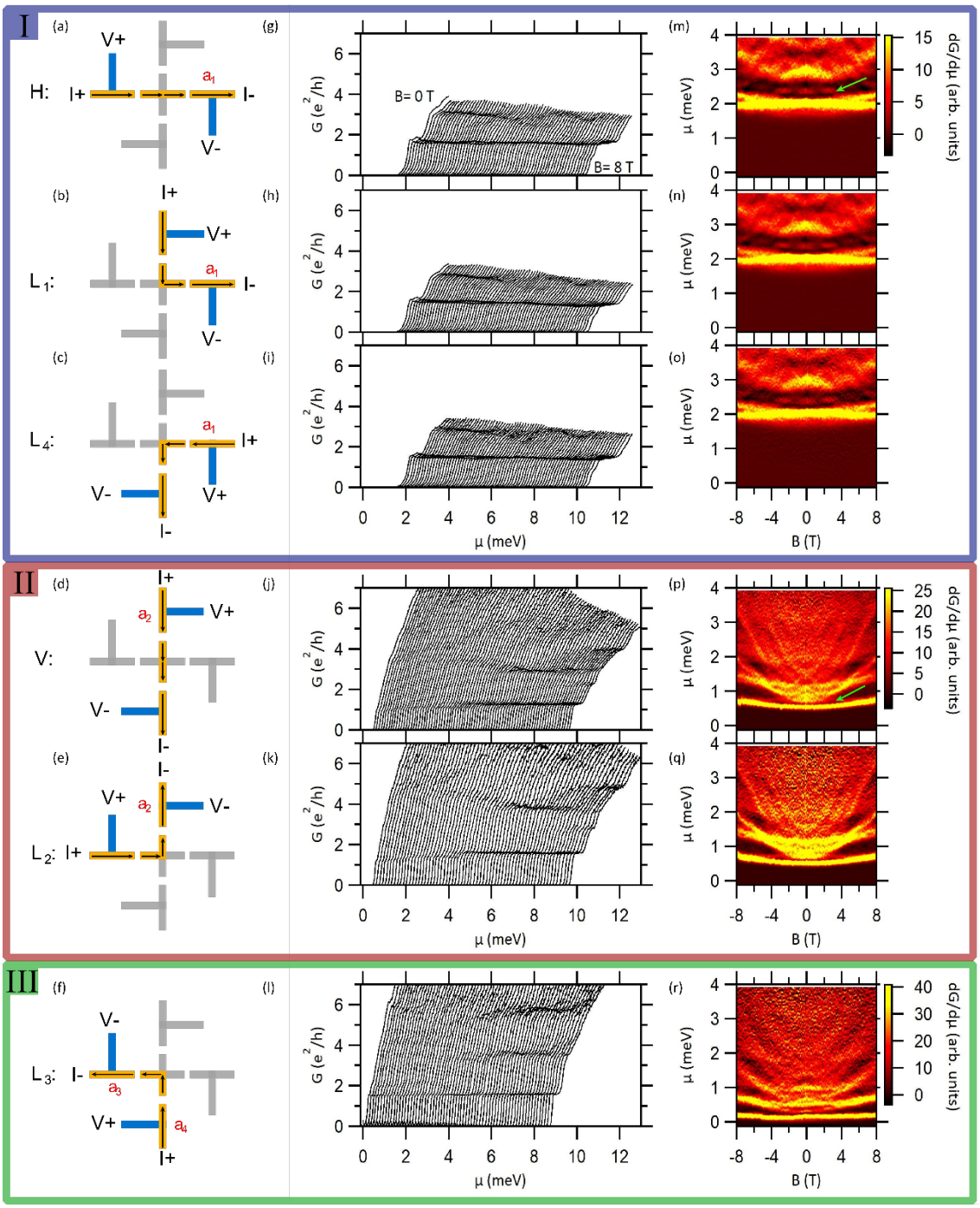

Fig. 2 Longitudinal magnetoconductance measurements for the six configurations of the nanocross of Device A at $\phi = 65°$, grouped on the basis of similar transconductance spectra. (a, d) Straight paths of the nanocross, (b, c, e, f) L-shaped paths of the nanocross, (g-l) Zero-bias longitudinal conductance, G, as a function of chemical potential μ and magnetic field B in the range $0 - 8$ T for the six configurations respectively. Data is shifted along x axis for clarity, (m-r) Transconductance spectra $dG/d\mu$ shown as a function of μ and B for the six configurations. The green arrows illustrate signatures of universal conductance fluctuations.

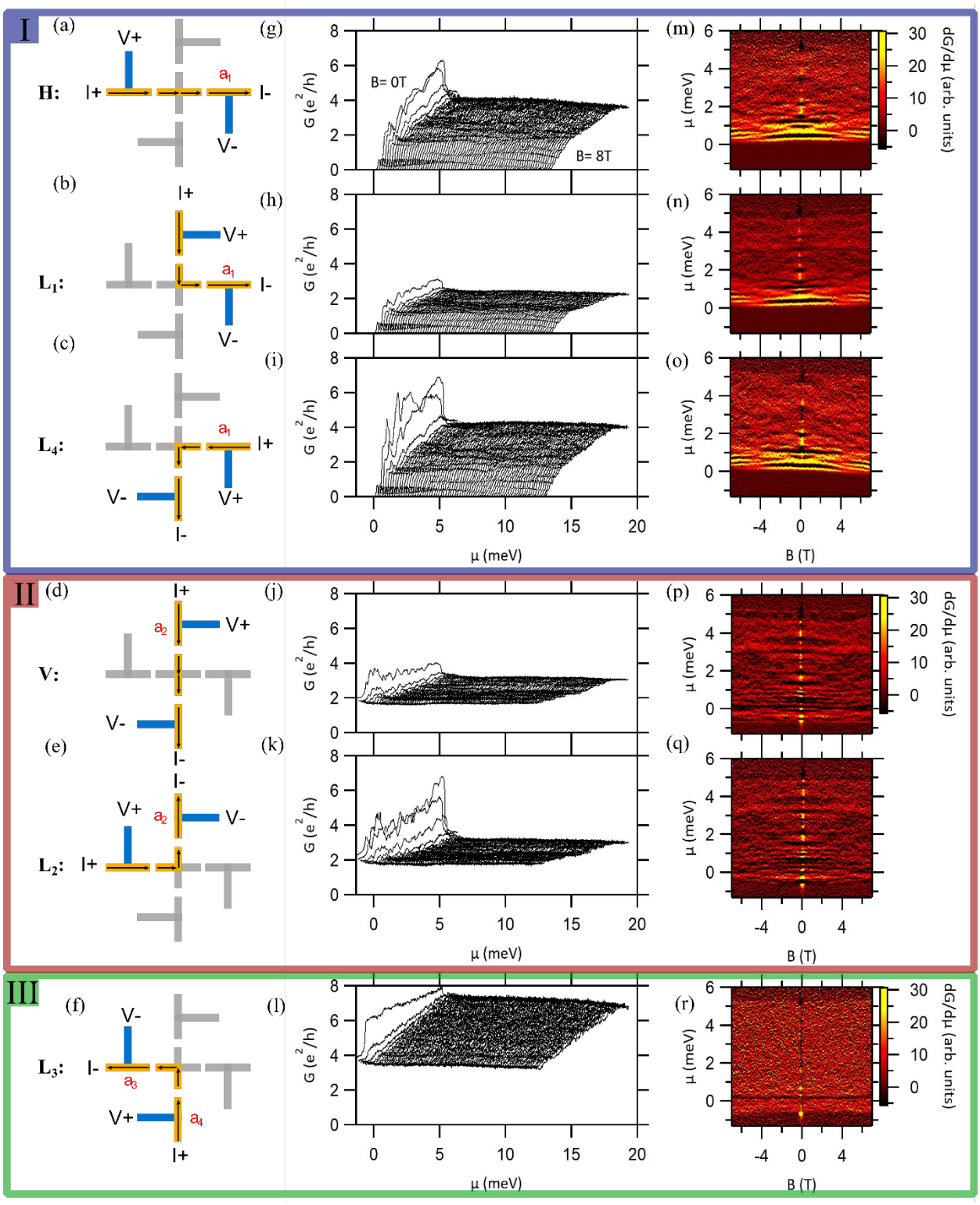

Fig. 3 Longitudinal magnetoconductance measurements for the six configurations of the nanocross of Device D, at $\phi = 0°$, grouped on the basis of similar transconductance spectra. (a, d) Straight paths of the nanocross, (b, c, e, f) L-shaped paths of the nanocross, (g-l) Zero-bias longitudinal conductance, G, as a function of chemical potential μ and magnetic field B in the range $0 - 8$ T for the six configurations respectively. Data is shifted along x axis for clarity, (m-r) Transconductance spectra $dG/d\mu$ shown as a function of μ and B for the six configurations.

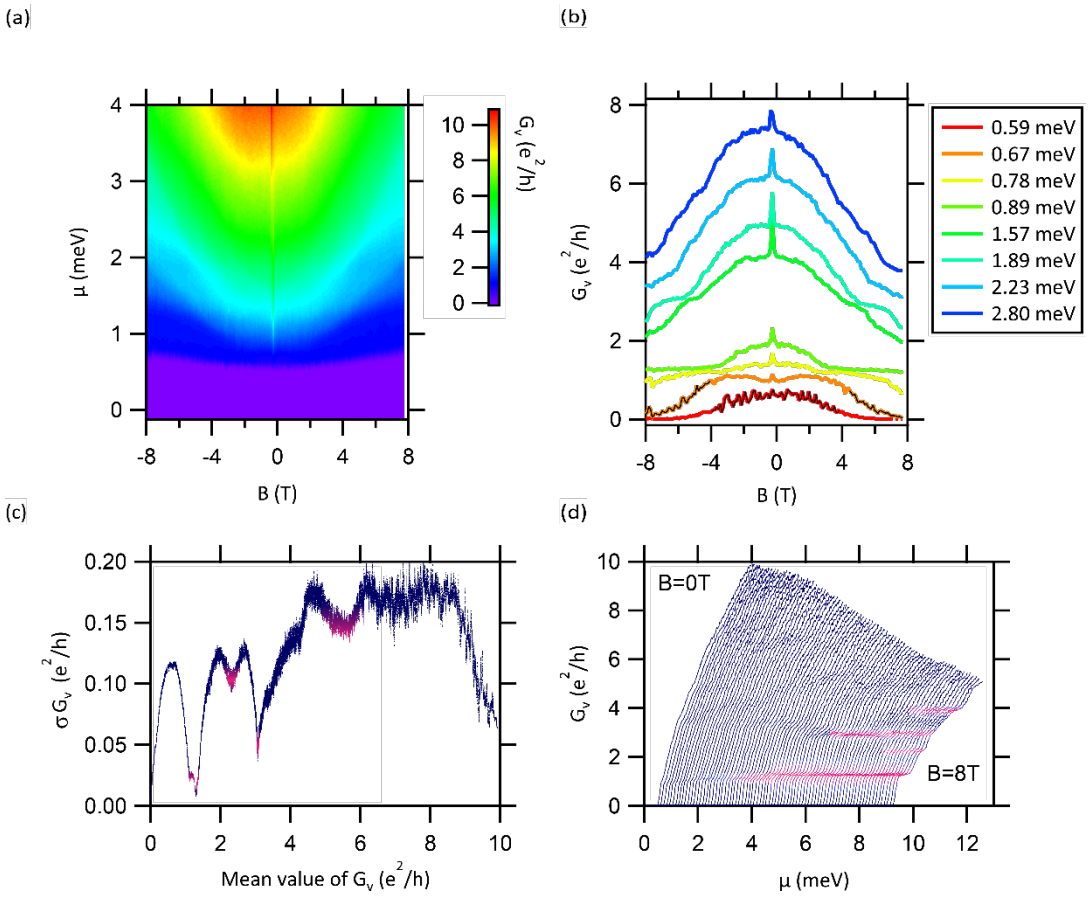

Fig. 4 Conductance (G_v) of the vertical configuration (V) and signatures of universal conductance fluctuations (UCF) for the vertical (V) configuration. (a) G_v intensity plot as a function of chemical potential μ and magnetic field B, (b) Line cuts of G_v intensity plot as a function of B at selected values of μ. Black lines highlight the quasi-oscillatory features of UCF, (c) Standard deviation of G_v (σG_v) as a function the mean value of G_v, (d) G_v as a function of the chemical potential μ with $B = 0$ T to 8 T. Dips in (c) corresponds to plateaus in (d) (shaded pink). Data is shifted along x axis for clarity.

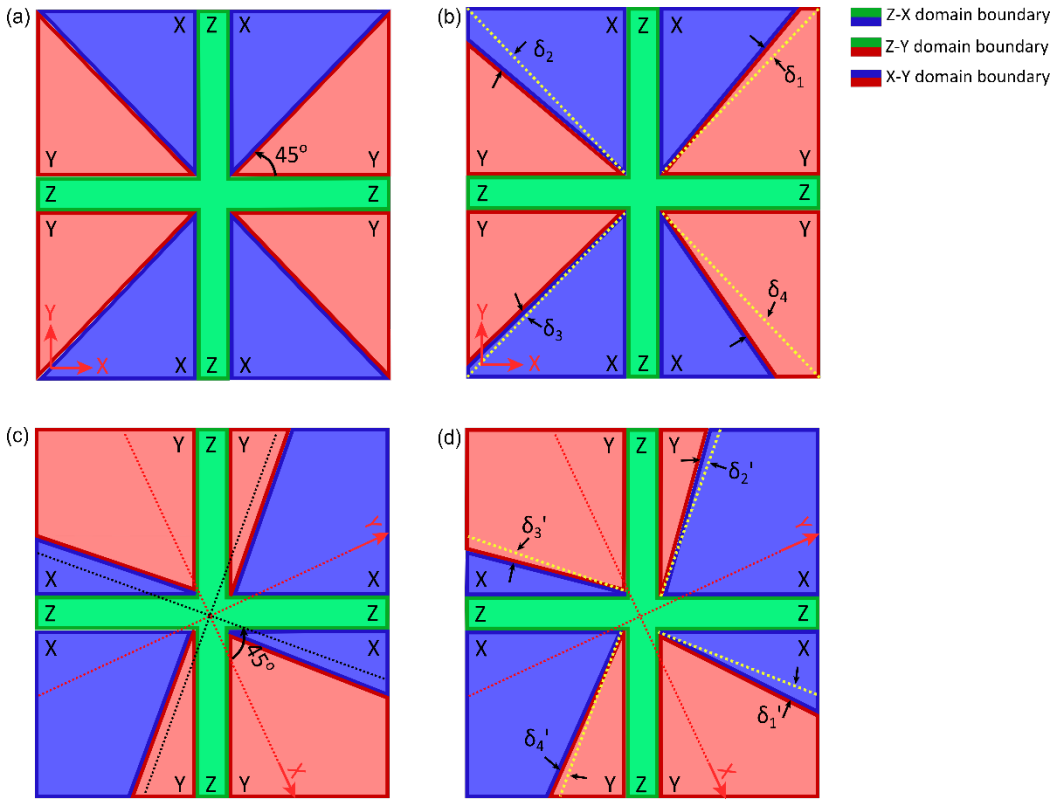

Fig. 5 Ferroelastic domain configuration for the two orientations of the nanocross: (a) The domain configuration of a symmetric nanocross in the lowest energy configuration when oriented along the crystallographic direction (Device D), (b) Expansion or contraction of the X and Y domains due to the presence of far-off boundary conditions producing a strain across the nanocross. For the given case $\delta_1, \delta_2 > 0$ and $\delta_3, \delta_4 < 0$. (c) The domain configuration of a symmetric nanocross in the lowest energy configuration when rotated by $\phi = 65°$ (Device A, B, C), (d) Expansion or contraction of the X and Y domains due to the presence of far-off boundary conditions producing a strain across the nanocross. For the given case $\delta_2', \delta_3' > 0$ and $\delta_1', \delta_4' < 0$. The Z-X, Z-Y and X-Y domain boundaries have been defined by darker shades along the edges of the nanocross for all cases.

References

1. Y.-Y. Pai, A. Tylan-Tyler, P. Irvin and J. Levy, *Rep Prog Phys*, 2018, **81**, 036503.
2. J. A. Sulpizio, S. Ilani, P. Irvin and J. Levy, *Annual Review of Materials Research*, 2014, **44**, 117.
3. A. Ohtomo and H. Y. Hwang, *Nature*, 2004, **427**, 423-426.
4. N. Reyren, S. Thiel, A. D. Caviglia, L. F. Kourkoutis, G. Hammerl, C. Richter, C. W. Schneider, T. Kopp, A. S. Ruetschi, D. Jaccard, M. Gabay, D. A. Muller, J. M. Triscone and J. Mannhart, *Science*, 2007, **317**, 1196-1199.
5. A. D. Caviglia, S. Gariglio, N. Reyren, D. Jaccard, T. Schneider, M. Gabay, S. Thiel, G. Hammerl, J. Mannhart and J. M. Triscone, *Nature*, 2008, **456**, 624-627.
6. A. Brinkman, M. Huijben, M. Van Zalk, J. Huijben, U. Zeitler, J. C. Maan, W. G. Van der Wiel, G. Rijnders, D. H. A. Blank and H. Hilgenkamp, *Nature Materials*, 2007, **6**, 493-496.
7. G. Cheng, M. Tomczyk, A. B. Tacla, H. Lee, S. Lu, J. P. Veazey, M. Huang, P. Irvin, S. Ryu, C.-B. Eom, A. Daley, D. Pekker and J. Levy, *Physical Review X*, 2016, **6**, 041042.
8. A. D. Caviglia, M. Gabay, S. Gariglio, N. Reyren, C. Cancellieri and J. M. Triscone, *Phys Rev Lett*, 2010, **104**, 126803.
9. M. Ben Shalom, M. Sachs, D. Rakhmilevitch, A. Palevski and Y. Dagan, *Phys Rev Lett*, 2010, **104**, 126802.
10. C. Cen, S. Thiel, J. Mannhart and J. Levy, *Science*, 2009, **323**, 1026-1030.
11. A. Annadi, G. Cheng, H. Lee, J.-W. Lee, S. Lu, A. Tylan-Tyler, M. Briggeman, M. Tomczyk, M. Huang, D. Pekker, C.-B. Eom, P. Irvin and J. Levy, *Nano Lett*, 2018, **18**, 4473-4481.
12. G. Cheng, M. Tomczyk, S. Lu, J. P. Veazey, M. Huang, P. Irvin, S. Ryu, H. Lee, C. B. Eom, C. S. Hellberg and J. Levy, *Nature*, 2015, **521**, 196.
13. Y.-Y. Pai, H. Lee, J.-W. Lee, A. Annadi, G. Cheng, S. Lu, M. Tomczyk, M. Huang, C.-B. Eom, P. Irvin and J. Levy, *Phys Rev Lett*, 2018, **120**, 147001.
14. Y. Frenkel, N. Haham, Y. Shperber, C. Bell, Y. Xie, Z. Chen, Y. Hikita, H. Y. Hwang and B. Kalisky, *ACS Applied Materials & Interfaces*, 2016, **8**, 12514-12519.
15. N. J. Goble, R. Akrobetu, H. Zaid, S. Sucharitakul, M.-H. Berger, A. Sehirlioglu and X. P. A. Gao, *Scientific Reports*, 2017, **7**, 44361.
16. R. A. Cowley, *Phys Rev*, 1964, **134**, A981-A997.
17. Y. Frenkel, N. Haham, Y. Shperber, C. Bell, Y. Xie, Z. Chen, Y. Hikita, H. Y. Hwang, E. K. H. Salje and B. Kalisky, *Nature Materials*, 2017, **16**, 1203-1208.
18. B. Kalisky, E. M. Spanton, H. Noad, J. R. Kirtley, K. C. Nowack, C. Bell, H. K. Sato, M. Hosoda, Y. Xie, Y. Hikita, C. Woltmann, G. Pfanzelt, R. Jany, C. Richter, H. Y. Hwang, J. Mannhart and K. A. Moler, *Nature Materials*, 2013, **12**, 1091-1095.
19. M. Honig, J. A. Sulpizio, J. Drori, A. Joshua, E. Zeldov and S. Ilani, *Nature Materials*, 2013, **12**, 1112-1118.
20. G. Cheng, A. Annadi, S. Lu, H. Lee, J.-W. Lee, M. Huang, C.-B. Eom, P. Irvin and J. Levy, *Phys Rev Lett*, 2018, **120**, 076801.
21. H. Noad, E. M. Spanton, K. C. Nowack, H. Inoue, M. Kim, T. A. Merz, C. Bell, Y. Hikita, R. Xu, W. Liu, A. Vailionis, H. Y. Hwang and K. A. Moler, *Phys Rev B*, 2016, **94**, 174516.

22. M. Ben Shalom, C. W. Tai, Y. Lereah, M. Sachs, E. Levy, D. Rakhmilevitch, A. Palevski and Y. Dagan, *Phys Rev B*, 2009, **80**, 140403.
23. A. Annadi, Z. Huang, K. Gopinadhan, X. R. Wang, A. Srivastava, Z. Q. Liu, H. H. Ma, T. P. Sarkar, T. Venkatesan and Ariando, *Phys Rev B*, 2013, **87**, 201102.
24. S. Seri and L. Klein, *Phys Rev B*, 2009, **80**, 180410.
25. H.-L. Hu, R. Zeng, A. Pham, T. T. Tan, Z. Chen, C. Kong, D. Wang and S. Li, *ACS Applied Materials & Interfaces*, 2016, DOI: 10.1021/acsami.6b01518, 13630–13636.
26. C. Cen, S. Thiel, G. Hammerl, C. W. Schneider, K. E. Andersen, C. S. Hellberg, J. Mannhart and J. Levy, *Nature Materials*, 2008, **7**, 298-302.
27. M. Huang, F. Bi, S. Ryu, C.-B. Eom, P. Irvin and J. Levy, *Apl Mater*, 2013, **1**, 052110.
28. G. Cheng, P. F. Siles, F. Bi, C. Cen, D. F. Bogorin, C. W. Bark, C. M. Folkman, J. W. Park, C. B. Eom, G. Medeiros-Ribeiro and J. Levy, *Nat Nanotechnol*, 2011, **6**, 343-347.
29. F. Bi, D. F. Bogorin, C. Cen, C. W. Bark, J. W. Park, C. B. Eom and J. Levy, *Applied Physics Letters*, 2010, **97**, 173110.
30. G. Timp, A. M. Chang, P. Mankiewich, R. Behringer, J. E. Cunningham, T. Y. Chang and R. E. Howard, *Phys Rev Lett*, 1987, **59**, 732-735.
31. T. Giamarchi and H. J. Schulz, *Phys Rev B*, 1988, **37**, 325-340.
32. C. L. Kane and M. P. A. Fisher, *Phys Rev B*, 1992, **46**, 15233-15262.
33. A. D. Stone, *Phys Rev Lett*, 1985, **54**, 2692-2695.
34. P. A. Lee and A. D. Stone, *Phys Rev Lett*, 1985, **55**, 1622-1625.
35. D. Rakhmilevitch, M. Ben Shalom, M. Eshkol, A. Tsukernik, A. Palevski and Y. Dagan, *Phys Rev B*, 2010, **82**.
36. B. Ludoph, M. H. Devoret, D. Esteve, C. Urbina and J. M. van Ruitenbeek, *Phys Rev Lett*, 1999, **82**, 1530-1533.
37. D. L. Maslov, C. Barnes and G. Kirczenow, *Phys Rev B*, 1993, **48**, 2543-2552.
38. P. Irvin, H. Lee, M. Briggeman, S. Liu, A. Annadi, G. Cheng, M. Tomczyk, M. Huang, C.-B. Eom and J. Levy, *in preparation*, 2017.
39. E. Heifets, E. Kotomin and V. A. Trepakov, *Journal of Physics: Condensed Matter*, 2006, **18**, 4845.
40. F. Xue, Y. Li, Y. Gu, J. Zhang and L.-Q. Chen, *Phys Rev B*, 2016, **94**, 220101.
41. J.-J. Wang, B. Wang and L.-Q. Chen, *Annual Review of Materials Research*, 2019, **49**, null.